A SEMI-CONVERGENT STAGE-WISE FRAMEWORK WITH PROVABLE GLOBAL CONVERGENCE FOR ADAPTIVE TOTAL VARIATION REGULARIZATION*

LIANG LUO † AND LEI ZHANG[‡]

Abstract. Image restoration requires a careful balance between noise suppression and structure preservation. While first-order total variation (TV) regularization effectively preserves edges, it often introduces staircase artifacts, whereas higher-order TV removes such artifacts but oversmooths fine details. To reconcile these competing effects, we propose a semi-convergent stage-wise framework that sequentially integrates first- and higher-order TV regularizers within an iterative restoration process implemented via ADMM. Each stage exhibits semi-convergence behavior—the iterates initially approach the ground truth before being degraded by over-regularization. By monitoring this evolution, the algorithm adaptively selects the locally optimal iterate (e.g., with the highest PSNR) and propagates it as the initial point for the next stage. This select-and-propagate mechanism effectively transfers local semi-convergence into a globally convergent iterative process. We establish theoretical guarantees showing that the sequence of stage-wise iterates is bounded, the objective values decrease monotonically. Extensive numerical experiments on denoising and deblurring benchmarks confirm that the proposed method achieves superior quantitative and perceptual performance compared with conventional first-, higher-order, hybrid TV methods, and learning based methods, while maintaining theoretical interpretability and algorithmic simplicity.

 $\textbf{Key words.} \ \ \textbf{Image restoration, Iterative regularization, Semi-convergence, Stage-wise optimization}$

MSC codes. 68U10, 49M27, 68U05

1. Introduction. Image restoration is a fundamental task in image processing, aiming to recover a clean image from its noisy observation while preserving critical details. In traditional approaches, whether based on linear filters or variational models, noise can be effectively reduced. However, these methods may blur fine structures or introduce artifacts, especially when dealing with high-level noise [1, 3, 25]. To achieving a good balance between noise reduction and structure preservation remains a significant challenge.

Let $u \in \mathbb{R}^{MN \times 1}$ and $f \in \mathbb{R}^{MN \times 1}$ denote respectively the desired image and the degraded image. Then, the degraded image f can be turned into the following inverse problem.

$$(1.1) f = Ku + \eta,$$

where $\eta \in \mathbb{R}^{MN \times 1}$ denotes the Gaussian white noise and $K \in \mathbb{R}^{MN \times MN}$ represents the blurred operator.

Due to the reconstruction of the desired image u is a severely ill-posed problem, it is not possible to obtain a unique solution [7, 11]. In order to address the issue, regularization techniques are employed. These techniques introduce additional constraints or prior knowledge into the model, which helps stabilize the inversion process

^{*}Submitted to the editors DATE.

Funding: This work is supported by the Zhejiang Provincial Natural Science Foundation under Grants LZ23A010006 and LY23A010004, NNSF of China under Grant 12271482, Research Grant of Zhejiang University of Technology 2022109001429.

[†]School of Mathematical Sciences, Zhejiang University of Technology, Hangzhou, China (ll-math09@163.com).

 $^{^{\}ddagger} \text{Corresponding}$ author, School of Mathematical Sciences, Zhejiang University of Technology, Hangzhou, China (zhanglei@zjut.edu.cn) .

and ensures that the solution is meaningful and well-posed [4, 15]. By penalizing undesirable features, regularization guides the solution toward a more robust and realistic result. For image restoration, we usually describe it using the following optimization problem.

(1.2)
$$u = \arg\min_{u} \mathcal{L}(Ku, f) + \lambda \phi(u)$$

where $\mathcal{L}(Ku, f)$ denotes data fidelity, $\lambda > 0$ represents the regularization parameter, and $\phi(u)$ denotes the regularization function.

In problem (1.2), the similarity between the observed image and the estimated image is guaranteed by the data fidelity term. The regularization term encodes prior knowledge and helps to extract important structural information from the image. Among various regularization techniques, the TV regularization, originally proposed by Rudin et al. [30], has become one of the most influential methods in image processing. It is formulated as follows.

(1.3)
$$u = \arg\min_{u} \frac{1}{2} ||Ku - f||_{2}^{2} + \lambda \phi(Du)$$

where $\phi(Du) = \sum_{i \leq M, j \leq N} |(Du)_{i,j}|$ and K denotes a convolution i.e., a blurring matrix. For image denoising task, K is the identity operator.

By using first-order TV regularization, some satisfactory results have been obtained in image denoising and edge preservation[13, 18]. However, such a model tends to produce blocky artifacts in uniform regions, which will significantly degrade image quality [28, 35, 36]. To address this drawback, several methods have been developed and have shown promising results in suppressing such artifacts while achieving better image restoration quality [20, 2, 6, 9]. Among these, the most fundamental higher-order TV model was introduced by Lysaker et al. [21], and it can be written as

(1.4)
$$u = \arg\min_{u} \frac{1}{2} ||Ku - f||_{2}^{2} + \lambda \phi(DDu)$$

where
$$\phi(DDu) = \sum_{i \leq M, j \leq N} |(DDu)_{i,j}|$$
.

The higher-order TV model (1.4) exceeds the first-order TV model (1.3), the limitations of higher-order TV regularization have been indicated, showing that these methods may degrade edge sharpness and lead to the loss of fine textural details [29].

Building upon the aforementioned models, an iterative image restoration (IIR) method [22] was proposed, utilizing initially a weighting function θ to combine the outputs of the first- and higher- order TV models. This hybrid approach leverages the complementary strengths of both models to achieve a trade-off between noise reduction and artifact suppression. Motivated by this idea, parallel hybrid approaches that combine the first-order TV term with higher-order TV terms and overlapping group sparsity (OGS) were proposed in [19, 27, 26, 17, 29, 8]. These methods can reduce noise, avoid artifacts in smooth regions, and achieve better restoration results.

Although significant progress has been made in optimizing regularization terms in existing research, the semi-convergence problem of iterative methods in image denoising cannot be effectively avoided. In this work, we propose a novel stage-wise image denoising framework that combines the strengths of both first-order and higher-order TV regularizations. In each stage of the framework, these two regularization models

are applied sequentially within an ADMM optimization scheme. The design is motivated by the complementary characteristics of first- and higher-order TV: the former excels at preserving sharp edges, while the latter suppresses staircase artifacts and residual noise.

A key feature of the proposed method lies in its semi-convergent refinement strategy. Specifically, we exploit the semi-convergence properties of iterative regularization by monitoring the PSNR evolution within each stage: the intermediate result with the higher PSNR is regarded as a locally optimal solution, which serves as the initial guess for the subsequent stage. This strategy allows the overall process to adaptively refine the reconstruction and improves stability. We further establish the convergence of this stage-wise process both theoretically and numerically, and extensive experiments on standard benchmarks show that our method consistently outperforms single-model TV-based baselines in both quantitative metrics (e.g., PSNR, SSIM, FOM) and visual quality.

The remainder of this paper is structured as follows. Section 2 reviews the necessary preliminaries and the ADMM framework. Section 3 discusses the optimization procedure for the proposed method and provides a theoretical convergence analysis. Section 4 presents numerical experiments to validate the convergence behavior and restoration performance of the proposed framework. Finally, Section 5 summarizes the work and presents directions for future research.

- **2. Preliminary.** A digital image can be modeled as a two-dimensional function u(i,j), where i and j denote respectively the spatial coordinates. For the image of size $n = M \times N$, its discrete representation will form a matrix. In typical practice, the image is vectorized into an n-dimensional column vector. In the following subsection, we introduce some basic notions and review ADMM algorithms.
- **2.1. The Notion of TV Operators.** The discrete first-order and second-order gradient operators, denoted respectively as D and DD, are constructed following the formulation presented in Wu and Tai [32]. Accordingly, the first-order discrete gradient $(Du)_{i,j}$ is given by

$$(2.1) (Du)_{i,j} = ((D_x^+ u)_{i,j}, (D_y^+ u)_{i,j})$$

where D_x^+u and D_y^+u are the first-order forward differences defined respectively as

(2.2)
$$(D_x^+ u)_{i,j} = \begin{cases} u_{i,j+1} - u_{i,j}, & 1 \le j \le N - 1 \\ u_{i,1} - u_{i,N}, & j = N \end{cases}$$

(2.3)
$$(D_y^+ u)_{i,j} = \begin{cases} u_{i+1,j} - u_{i,j}, & 1 \le i \le M - 1 \\ u_{1,j} - u_{N,j}, & i = M \end{cases}$$

and the first-order backward differences D_x^-u and D_y^-u separately are

(2.4)
$$(D_x^- u)_{i,j} = \begin{cases} u_{i,j} - u_{i,j-1}, & 1 < j \le N \\ u_{i,1} - u_{i,N}, & j = 1 \end{cases}$$

(2.5)
$$(D_y^- u)_{i,j} = \begin{cases} u_{i,j} - u_{i-1,j}, & 1 \le i \le N \\ u_{1,j} - u_{n,j}, & i = 1 \end{cases}$$

and the second-order discrete gradient $(DDu)_{i,j}$ can be described as

$$(2.6) (DDu)_{i,j} = \begin{pmatrix} D_x^-(D_x^+u_{i,j}) & D_y^+(D_x^+u_{i,j}) \\ D_x^+(D_y^+u_{i,j}) & D_y^-(D_y^+u_{i,j}) \end{pmatrix}$$

Detailed definitions of the discrete second-order gradient operators $D_x^-(D_x^+)$, $D_y^+(D_x^+)$, $D_x^+(D_y^+)$, and $D_y^-(D_y^+)$ can be found in [32].

2.2. ADMM algorithm. As an enhanced variant of the classical augmented Lagrangian approach [12], the alternating direction method of multipliers (ADMM) [14, 33] decomposes multi-variable optimization tasks into smaller sub-problems for iterative solutions. ADMM has been shown to be highly effective for constrained convex optimization problems with separable structures, due to this decomposition framework.

(2.7)
$$\min_{x,z} f(x) + g(z), \text{ s.t. } Ax + Bz = c.$$

where $f(\cdot)$, $g(\cdot)$ are closed convex functions, $A \in \mathbb{R}^{p \times n}$, $B \in \mathbb{R}^{p \times m}$ are linear operator, $x \in \mathbb{R}^n$, $z \in \mathbb{R}^m$ are elements of nonempty closed convex sets, $c \in \mathbb{R}^p$ represents a given vector. The augmented Lagrangian function corresponding to problem (2.7) takes the form

(2.8)
$$L_{\rho}(x,z,\mu) = f(x) + g(z) - \mu^{T}(Ax + Bz - c) + \frac{\rho}{2} ||Ax + Bz - c||_{2}^{2}$$

where $\mu \in \mathbb{R}^p$ denotes the Lagrange multiplier and $\rho > 0$ is the penalty parameter.

The saddle point of problem (2.8) is achieved by alternatively minimizing L_{ρ} over x, z, and μ . The ADMM algorithm for optimizing problem (2.7) is outlined in Algorithm 2.1.

Algorithm 2.1 ADMM for the optimization problem (2.7)

```
Initialize x^0, z^0, \mu^0 and \rho > 0. while stopping condition is not satisfied do x^{k+1} = \arg\min_x \left( f(x) + \frac{\rho}{2} \|Ax + Bz - c + \frac{\mu^k}{\rho}\|_2^2 \right) \; // \; \text{Update} \; x z^{k+1} = \arg\min_z \left( g(z) + \frac{\rho}{2} \|Ax^{k+1} + Bz - c + \frac{\mu^k}{\rho}\|_2^2 \right) \; // \; \text{Update} \; z \mu^{k+1} = \mu^k + \rho (Ax^{k+1} + Bz^{k+1} - c) \; // \; \text{Update} \; \mu k = k+1 end while return x^{k+1}
```

3. Related work. To formulate the restoration framework, we propose a hybrid regularization model that alternates between first-order and higher-order TV terms. For convenience, we introduce a switching function $\sigma(i)$. The objective function takes the following form:

(3.1)
$$\mathcal{J}(u) = \frac{1}{2} \|Ku - f\|_2^2 + \lambda_{\sigma(i)} \operatorname{TV}_{\sigma(i)}(u), \qquad i = 1, 2 \dots$$

where

$$\sigma(i) = \begin{cases} 1, & i \text{ is odd} \\ 2, & i \text{ is even} \end{cases}$$

which selects the type of TV regularizer used in the *i*-th stage. Specifically, $\text{TV}_1(u) = \phi(Du)$ and $\text{TV}_2(u) = \phi(DDu)$ denote respectively the first- and higher- order TV regularizer with λ_1 and λ_2 being their corresponding regularization weights. Here, K denotes the blurring operator and f is the degraded observation. The switching function $\sigma(i)$ ensures that the two regularizers are not minimized simultaneously but are instead updated sequentially in an alternating manner.

As the first step in our alternating optimization strategy, we first minimize the first-order TV sub-problem associated with the term $\lambda_1 \text{TV}_1(u)$. This is equivalent to solving the classical ROF model via the ADMM algorithm described in [32], and the details are given in Algorithm 3.1.

Algorithm 3.1 ADMM for the optimization problem (1.3)

```
Require f, K and parameters \lambda > 0, \omega > 0.

Initialize u_0 = f, k = 0, \rho = 2, y_i = 0 for i = 1, 2.

while stopping condition is not satisfied do u^{k+1} = \mathcal{F}^{-1}(\frac{\mathcal{F}(K^T)\mathcal{F}(f) - \mathcal{F}(D^T)\mathcal{F}(\rho v^k + y^k)}{\mathcal{F}(K^T)\mathcal{F}(K) + \rho \mathcal{F}(D^T)\mathcal{F}(D)}) \text{ // Update } x
v^{k+1} = \max\left\{0, \|x^{k+1}\|_2 - \frac{\lambda}{\rho}\right\} \cdot sign(x^{k+1}) \text{ // Update } v
y^{k+1} = y^k + \rho(v^{k+1} - Du^{k+1}) \text{ // Update } y
k = k+1
end while
\text{return } x^{k+1}
```

The restored result from the first-order TV sub-problem is then passed to the second stage, where we solve the higher-order TV sub-problem corresponding to the term $\lambda_2 \text{TV}_2(u)$. This stage aims to further suppress staircase artifacts and enhance smoothness in homogeneous regions. To achieve this, we formulate the second-stage problem as the minimization of the following energy functional:

(3.2)
$$\min_{u} \frac{1}{2} ||Ku - f||_{2}^{2} + \lambda \cdot \phi(DDu)$$

where $\lambda > 0$ is the regularization parameter.

To facilitate solving problem (3.2), we define an intermediate variable v and recast the problem into a constrained formulation.

(3.3)
$$\min_{u,v} \frac{1}{2} ||Ku - f||_2^2 + \lambda \cdot \phi(v), \text{ s.t. } v = DDu.$$

The Lagrange multipliers μ and the penalty parameter β are introduced. Therefore, the augmented Lagrangian function of problem (3.3) is

(3.4)
$$L_{\beta}(u, v, \mu) = \frac{1}{2} \|Ku - f\|_{2}^{2} + \lambda \cdot \phi(v) - \mu^{T}(v - DDu) + \frac{\beta}{2} \|v - DDu\|_{2}^{2}$$

In problem (3.4), the intermediate variables v and Lagrange multipliers μ can be described as

(3.5)
$$v = [v_1, v_2, v_3, v_4]^T, \quad \mu = [\mu_1, \mu_2, \mu_3, \mu_4]^T$$

respectively, and

(3.6)
$$||v||_2 = \sum_{i \le M, j \le N} \sqrt{(v_1)_{i,j}^2 + (v_2)_{i,j}^2 + (v_3)_{i,j}^2 + (v_4)_{i,j}^2}$$

To obtain the saddle point of problem (3.4), we use the ADMM method to iteratively and alternately solve the following three sub-problems

(3.7)
$$\begin{cases} u^{k+1} = \arg\min_{u} \frac{1}{2} \|Ku - f\|_{2}^{2} - \langle \mu^{k}, v^{k} - DDu \rangle + \frac{\beta}{2} \|v^{k} - DDu\|_{2}^{2}, \\ v^{k+1} = \arg\min_{v} \lambda \cdot \phi(v) - \langle \mu^{k}, v - DDu^{k+1} \rangle + \frac{\beta}{2} \|v - DDu^{k+1}\|_{2}^{2}, \\ \mu^{k+1} = \mu^{k} - \beta(v^{k+1} - DDu^{k+1}). \end{cases}$$

The following steps provide a detailed solution process for the given problems.

3.1. u sub-problem. fixing v and μ , the sub-problem for u^{k+1} can be rewritten as:

(3.8)
$$u^{k+1} = \arg\min_{u} \frac{1}{2} ||Ku - f||_{2}^{2} + \frac{\beta}{2} ||v^{k} - DDu - \frac{\mu^{k}}{\beta}||_{2}^{2}$$

By solving the sub-problem (3.8), we have

$$(3.9) (K^T K + \beta (DD)^T DD) u^{k+1} = K^T f + \beta (DD)^T v^k - (DD)^T \mu^k$$

Since periodic boundary conditions are applied, and the matrices K^TK and $(DD)^TDD$ are block circulant [31], the linear system (3.9) can be efficiently solved using the Fast Fourier Transform (FFT), and the solution for u^{k+1} is obtained via element-wise division.

(3.10)
$$u^{k+1} = \mathcal{F}^{-1} \left(\frac{\mathcal{F}(K^T)\mathcal{F}(f) + \mathcal{F}(DD)^T \mathcal{F}(\beta v^k - \mu^k)}{\mathcal{F}(K^T)\mathcal{F}(K) + \beta \mathcal{F}(DD)^T \mathcal{F}(DD)} \right)$$

where \mathcal{F} and \mathcal{F}^{-1} respectively represent FFT and its inverse transform.

3.2. v sub-problem. fixing variable u and μ . The v-sub-problem can be rewritten as

(3.11)
$$v^{k+1} = \arg\min_{v} \lambda \cdot \phi(v) + \frac{\beta}{2} \left\| v - (DDu^{k+1} + \frac{\mu^{k}}{\beta}) \right\|_{2}^{2}$$

Let $x^{k+1} = DDu^{k+1} + \frac{\mu^k}{\beta}$, the solution of Problem (3.11) can be obtained using the well-known shrinkage formula.

(3.12)
$$v^{k+1} = \operatorname{shrink}(x^{k+1}, \frac{\lambda}{\beta}) = \max\{0, \|x^{k+1}\|_2 - \frac{\lambda}{\beta}\} \cdot \operatorname{sign}(x^{k+1})$$

where shrink (\cdot) denotes the shrinkage operator and $||x^{k+1}||_2$ is given by

(3.13)
$$||x^{k+1}||_2 = \sum_{i=1}^M \sum_{j=1}^N \sqrt{(x_1^{k+1})_{i,j}^2 + (x_2^{k+1})_{i,j}^2 + (x_3^{k+1})_{i,j}^2 + (x_4^{k+1})_{i,j}^2}$$

Hence, the detailed process for the higher-order TV model (1.4) is presented in Algorithm 3.2.

Building upon this, we propose a stage-wise alternating restoration algorithm, where each stage solves a variational problem with either first-order or high-order

Algorithm 3.2 ADMM for the optimization problem (1.4)

```
Require f, K and parameters \lambda > 0, \omega > 0.

Initialize u_0 = f, k = 0, \beta = 2 and \mu_j = 0 for j = 1, 2, 3, 4.

while stopping condition is not satisfied \mathbf{do}
u^{k+1} = \mathcal{F}^{-1} \left( \frac{\mathcal{F}(K^T)\mathcal{F}(f) + \mathcal{F}(DD^T)\mathcal{F}(\beta v^k - \mu^k)}{\mathcal{F}(K^T)\mathcal{F}(K) - \beta \mathcal{F}(DD^T)\mathcal{F}(DD^T)} \right) \text{ // Update } u
v^{k+1} = \max \left\{ 0, \|x^{k+1}\|_2 - \frac{\omega}{\beta} \right\} \cdot \text{sign}(x^{k+1}) \text{ // Update } v
\mu^{k+1} = \mu^k - \beta(v^{k+1} - DDu^{k+1}) \text{ // Update } \mu
k = k+1
end while
\mathbf{return} \quad u^{k+1}
```

total variation regularization. The alternation is governed by the principle of semiconvergence: once the residual stops decreasing and starts increasing, the iteration halts and transitions to the next stage. This strategy avoids overfitting noise and enables adaptivity to different image features. The full method alternates between the two stages until a total iteration cap is reached or the accuracy setting is achieved. The stage-wise alternating method proposed is succinctly summarized in Algorithm 3.3.

Algorithm 3.3 Stage-wise alternating framework for image restoration

Require Noisy image f, blurring operator K, regularization parameters λ_1, λ_2 , maximum outer iterations N_{max} .

```
imum outer iterations N_{\max}. Ensure Restored image u. Initialize u_0^{(k)} = f, k = 0, N = 1. while N \leq N_{\max} do u_N^{(k+1)} = \mathbf{Algorithm} \ \mathbf{2}(u_{N-1}^{(k)}, K, \lambda_1) \ // \ \text{First-order TV} \ \text{regularization stage} if \|Ku_N^{(k+1)} - f\| > \|Ku_N^{(k)} - f\| \ \text{then} Return u_N^{(k)} \ // \ \text{semi-convergence analysis} end if if N \geq N_{\max} \ \text{then} Return u_N^{(k)} \ // \ \text{Check} \ \text{if } N_{\max} \ \text{is reached} end if N \leftarrow N + 1 \ // \ N + 1 u_N^{(k+1)} = \mathbf{Algorithm} \ \mathbf{3}(u_{N-1}^{(k)}, K, \lambda_2) \ // \ \text{High-order TV} \ \text{regularization stage} if \|Ku_N^{(k+1)} - f\| > \|Ku_N^{(k)} - f\| \ \text{then} Return u_N^{(k)} \ // \ \text{semi-convergence analysis} end if if N \geq N_{\max} \ \text{then} Return u_N^{(k)} \ // \ \text{Check} \ \text{if } N_{\max} \ \text{is reached} end if N \leftarrow N + 1 \ // \ N + 1 \ \text{end while} return u_N^{(k)} \ // \ \text{Check} \ \text{if } N_{\max} \ \text{is reached} end while return u_N^{(k)} \ // \ \text{Check} \ \text{if } N_{\max} \ \text{is reached}
```

To facilitate the convergence analysis of the proposed algorithm, we introduce following notations.

we define $\mathcal{J}_1(u) = \lambda_1 T V_1(u)$, $\mathcal{J}_2(u) = \lambda_2 T V_2(u)$ and then the optimization problem (3.1) can be divided into independent two part

(3.14)
$$\min_{u} \mathcal{J}_{i}(u) + H(u), \quad i = 1, 2$$

where \mathcal{J}_i is proper, convex and lower semi-continuous, H is convex and continuously differentiable. At the same time, the approximation of problem is given as follows

(3.15)
$$\min_{u} \mathcal{J}(u) + \frac{\delta_k}{2} \|u - (u^k - \frac{1}{\delta_k} K^T (K u^k - f))\|_2^2$$

Building upon prior works in [10, 16, 34], we introduce the following lemmas.

LEMMA 3.1. Assume that H is Lipschitz continuous with associated Lipschitz constant L, u^* is the solution of problem (3.14), u^k is the solution of the problem (3.15). If, for each $M \in R$ there exists a constant $\sigma(M) > 0$ such that

(3.16)
$$\|\bar{v} - u^*\| \le \sigma(M)(R(\bar{v} + T(\bar{v})))$$

for each \bar{v} satisfying $(\mathcal{J} + H)(u) \leq M$ and $\bar{v}, R(\bar{v})$ and $T(\bar{v})$ defined by

(3.17)
$$\bar{v} = \arg\min_{v} \mathcal{J}(v) + \frac{\delta}{2} \|v - u + \frac{1}{\delta} H'(u)\|_{2}^{2}$$

(3.18)
$$R(\bar{v}) = \langle H'(u^*), \bar{v} - u^* \rangle + \mathcal{J}(\bar{v} - \mathcal{J}(u^*)),$$

(3.19)
$$T(\bar{v}) = H(\bar{v}) - H(u^*) - \langle H'(u^*), \bar{v} - u^* \rangle$$

then u^k converges linearly to the unique minimizer u^* .

LEMMA 3.2. The sequence of iterates $\{u^k\}$ generated by the ADMM Algorithm Algorithm 3.1 converges linearly to the solution of the problem (1.3).

LEMMA 3.3. The sequence of iterates $\{u^k\}$ generated by the ADMM Algorithm Algorithm 3.2 converges linearly to the solution of the problem (1.4).

For the purpose of analyzing the convergence of the proposed method, we assume the existence of a neighborhood $B(u, \delta)$ of the ground truth image u such that both optimal solutions u_1^* and u_2^* are contained in $B(u, \delta)$.

Theorem 3.4. The sequence of iterates $\{u_N^k\}$ converges to the neighborhood of ground image u, where the u_N^k is generated by the Algorithm 3.3.

Proof. Define that $\{u_N^k\}$ denotes the sequence generated by Algorithm 3.3 at the k-th iteration of the N-th stage. Let u_1^* and u_2^* denote respectively the solutions of the minimization problem (1.3) and problem (1.4). Moreover, let u denote the ground truth image. By Lemma 3.2, Lemma 3.3 and the above assumptions, we proceed to prove the theorem as follows.

$$(3.20) ||u_N^k - u|| = ||u_N^k - u_1^* + u_1^* - u_2^* + u_2^* - u||$$

$$\leq ||u_N^k - u_1^*|| + ||u_1^* - u_2^*|| + ||u_2^* - u||$$

$$\leq ||u_N^k - u_1^*|| + 2\delta + \delta$$

(3.23)
$$\leq \sigma + 3\delta$$
 where $N = 2n - 1, n = 1, 2, 3, \cdots$

$$(3.24) ||u_N^k - u|| = ||u_N^k - u_2^* + u_2^* - u_1^* + u_1^* - u||$$

$$\leq ||u_N^k - u_2^*|| + ||u_2^* - u_1^*|| + ||u_1^* - u||$$

$$\leq ||u_N^k - u_2^*|| + 2\delta + \delta$$

(3.27)
$$\leq \sigma + 3\delta$$
 where $N = 2n, n = 1, 2, 3, \cdots$

According to the above discuss. we let $\hat{\delta} = \sigma + 3\delta$, then we have

$$||u_N^k - u|| < \hat{\delta} \quad \text{for all} \quad N$$

Therefore, the sequence $\{u_N^k\}$ generated by Algorithm 3.3 converges to the neighborhood of the ground image u. To better understand the convergence process of the alternating iteration, we have drawn the flow diagram of the graphical convergence process, as shown in Figure 1.

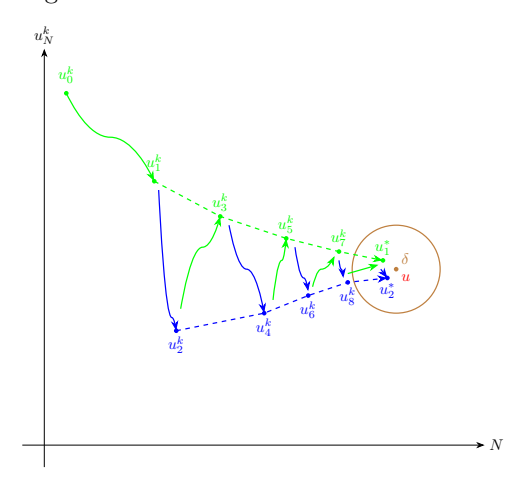


Fig. 1: The flow diagram of the graphical convergence process

Although the denoising framework is guided by the semi-convergence property to select intermediate iterates within each stage, Theorem 3.4 ensures that the overall iterative sequence u_N^k converges to a neighborhood of the ground image u. This result is particularly significant, as traditional TV-based denoising methods often lack such global convergence guarantees and rely solely on heuristic stopping rules. The proof, while concise, confirms that the proposed scheme remains stable under the stage-wise regularization strategy.

4. Numerical results. In order to assess the performance of our proposed approach, we carried out numerical experiments on the test images illustrated in Figure 2, considering three noise levels: $\sigma = 10$, $\sigma = 20$, and $\sigma = 30$. Furthermore, a 3×3 Gaussian kernel was applied to further blur the image. All experiments were performed on an Apple M1 with 8 GB of RAM. Practically, in this study, MATLAB (R2021b) is chosen to run the proposed procedure. PSNR [23], SSIM [5], and FOM [41] are the main quantitative analyses that are used to evaluate the proposed method.

We compared the proposed method with several existing TV models and methods, including the ROF model [30], the LLT model [21], the TGV model [9], the DBC-TV model [6] and the Nesterov's method [24]. In the original papers [30] and [21], the gradient descent scheme was used to solve the minimization problem. However, in our experiment, we employ the ADMM scheme [14] to improve the efficiency of the optimization process. Unlike standard gradient descent schemes, the ADMM framework reformulates the constrained optimization problem through decomposition into smaller sub-problems. These sub-problems are solved independently, leading to accelerated convergence and improved effectiveness for image restoration.

In all Algorithm, the stopping criterion was choosen as

(4.1)
$$e_r = \frac{\|u^{k+1} - u^k\|_2}{\|u^k\|_2} < \delta$$

where $\delta = 1 \times 10^{-8}$, u^{k+1} and u^k correspond to the restored image obtained in the

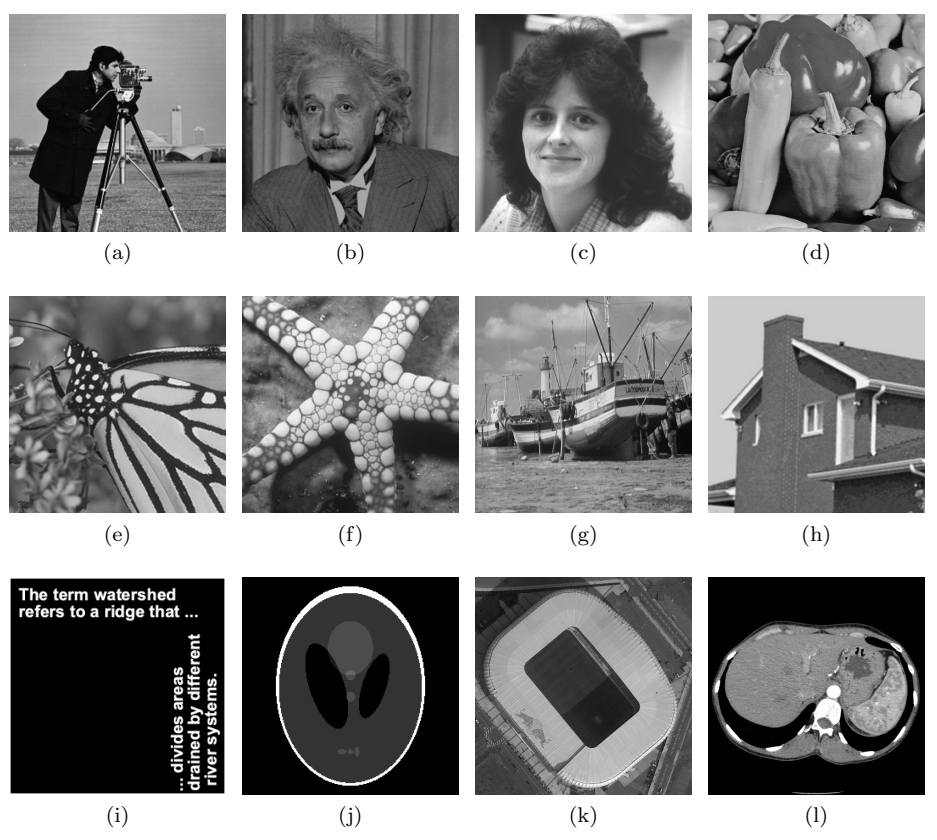


Fig. 2: The test images. (a) Cameraman (b) Einstein (c) Woman (d) Peppers (e) Butterfly (f) Starfish (g) Boat (h) House (i) Text (j) Logan (k) Stadium (l) Brain

present and the previous iterations, respectively.

In the proposed alternating optimization framework, the regularization terms $\lambda_1 \text{TV}_1(u)$ and $\lambda_2 \text{TV}_2(u)$ are not explicitly combined in a single objective function. Instead, each term is activated in a separate stage, and their relative influence is determined by an adaptive selection function $\sigma(i)$. Specifically, at each stage, both first- and higher- order TV sub-problems are solved independently. The restored result with the higher PSNR values is retained as the intermediate local optimal solution and used as an input for the next stage. This implicit selection mechanism allows the framework to dynamically balance edge preservation without requiring manual tuning of the relative weights λ_1 and λ_2 . In the numerical implementation, each sub-problem has its own regularization parameter λ used.

An appropriate choice of λ helps suppress artifacts while preserving sharp and natural textures. In our experiments, due to the alternating nature of our framework, a smaller λ leads to better PSNR performance. therefore, we empirically set $\lambda=2$. For the update of the parameter β , we adopt their original update strategy. Regarding the selection of the parameter α , we empirically choose $\alpha=0.618$.

To illustrate graphically the convergence behavior of the proposed stage-wise alternating method, we present the progression of PSNR, SSIM, and relative error metrics over the optimization iterations when $\sigma = 20$, as shown in Figures 3 and

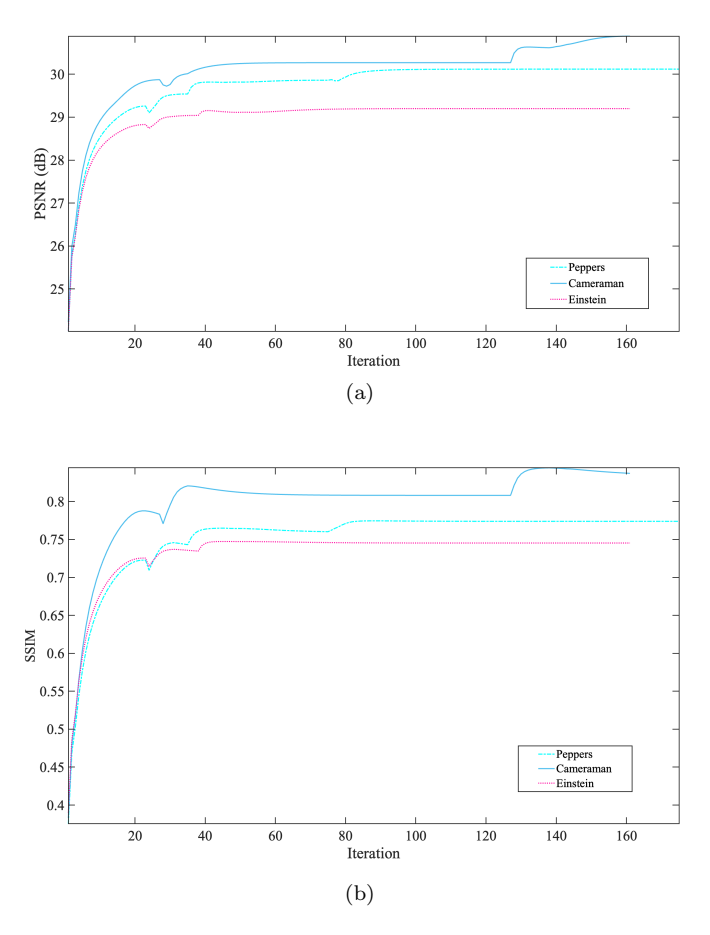


Fig. 3: A visual representation of convergence analysis.(a) PSNR curves for the Peppers, Cameraman, and Einstein images; (b) SSIM curves for the same images.

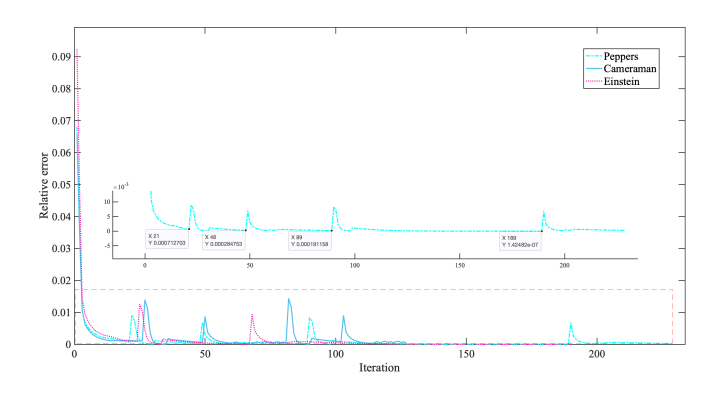


Fig. 4: Relative error curve for the Peppers, Cameraman, and Einstein images.

4. Although experiments were conducted on all images shown in Figure 2, only the Cameraman, Peppers, and Einstein images were selected as representative test cases for their rich textural details.

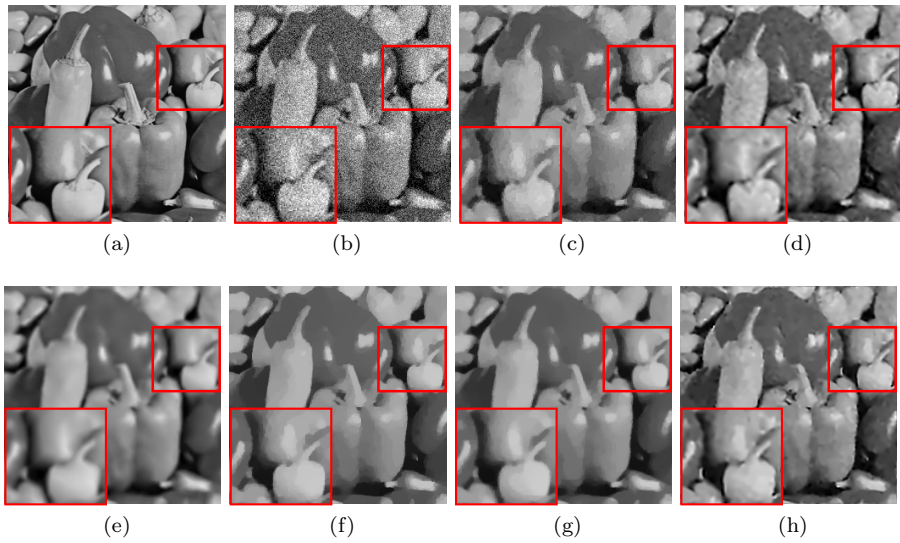


Fig. 5: Restored Peppers. (a)Original, (b)Degraded, (c)ROF model, (d)LLT model, (e)TGV model, (f)DBC-TV model, (g)Nesterov's method, and (h)Proposed method.

As observed, the PSNR and SSIM curves exhibit a slight temporary decline after a certain number of iterations, indicating the alternation of the regularizer. This is subsequently followed by a continued increase until a global optimum is reached. Empirical results indicate that the optimum is generally achieved after the 5-6 stages. Moreover, the relative error gradually decreases as the number of stages increases, ultimately demonstrating stable convergence.

Additionally, minor fluctuations in the relative error curve are observed throughout the iterative process, primarily resulting from differences in update strategies between the first-order TV regularization term and the higher-order TV regularization term. These fluctuations are particularly evident during the transition phase, where the TV model initially undergoes a brief adjustment period to accommodate newly imposed constraints. However, these transient fluctuations do not impede the overall convergence behavior. Rather, they reflect the algorithm's adaptive capacity to adjust and alternate between the two TV models, ensuring effective optimization.

Interestingly, in the case of the Peppers image, the first stage of the restoration procedure converges at the 21st iteration. During the subsequent iterations, the relative error curve exhibits temporary increases. Then, the second and third stages are completed at the 48th and 89th iterations, respectively, and the process ultimately converges at the 189th iteration. It is worth noting that the relative error at each stage becomes progressively lower than in the previous one, providing evidence for the convergence of the proposed method , which follows the theoretical convergence analysis shown in Figure 1.

Regarding the Cameraman image in Figure 6, which contains less edge information, all methods demonstrated effective denoising and satisfactory edge preservation, except for the ROF model [30], which exhibited residual artifacts, particularly on the cameraman's face. Comparative analysis indicates that the LLT model [21] achieves

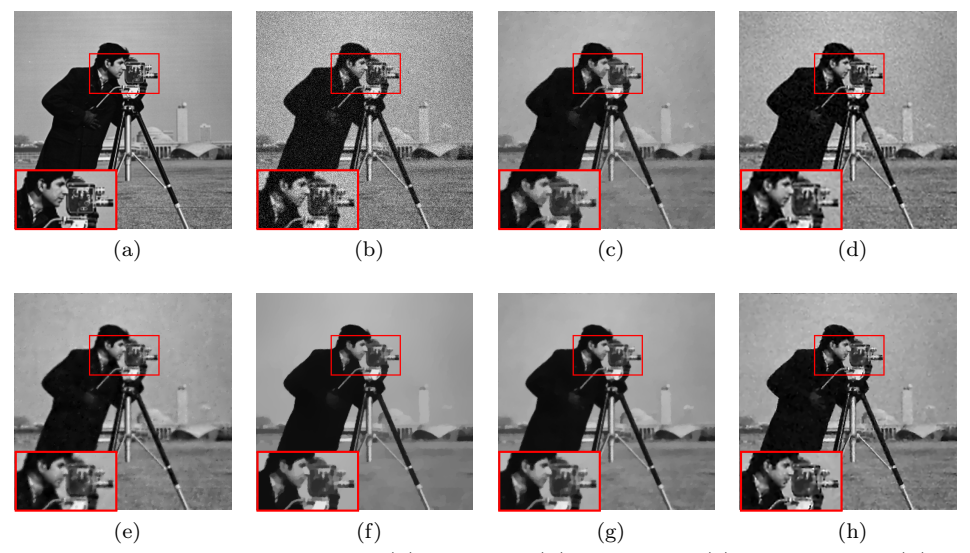


Fig. 6: Restored Cameraman. (a)Original, (b)Degraded, (c)ROF model, (d)LLT model, (e)TGV model, (f)DBC-TV model, (g)Nesterov's method, and (h)Proposed method.

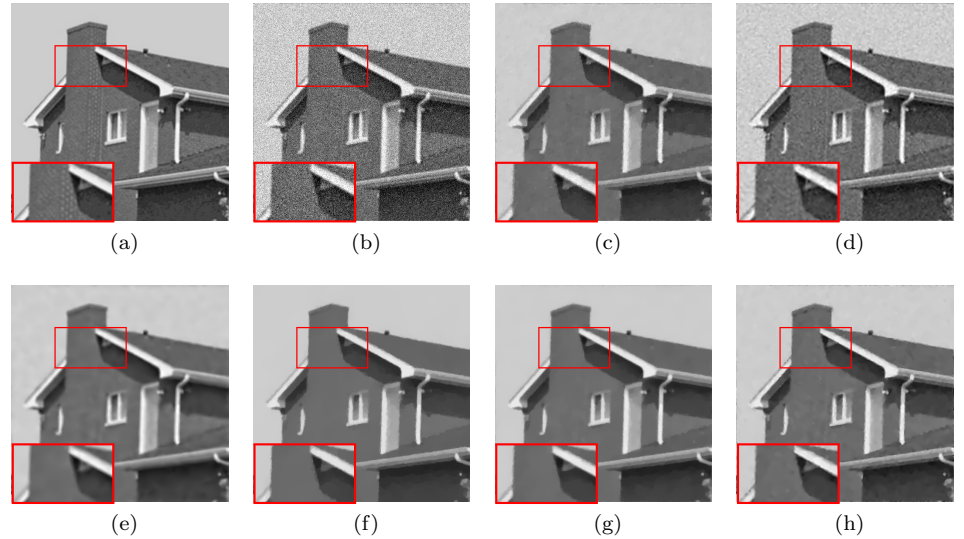


Fig. 7: Restored House. (a)Original, (b)Degraded, (c)ROF model, (d)LLT model, (e) TGV model, (f)DBC-TV model, (g)Nesterov's method, and (h)Proposed method.

superior edge preservation. However, our proposed method yields comparable performance in maintaining the important edge.

Meanwhile, the House image in Figure 7 features complex and rich edge structures and textures. Inspection of the zoomed-in region shows that all methods achieved effective denoising performance, although the ROF model [30] displayed residual artifacts. Comparative analysis of restored enlarged images reveals that, while the TGV

model [9] introduces slight blurring, it achieves the best overall restoration by effectively balancing denoising and edge preservation. Visually, our proposed method also produces satisfactory results, underscoring its competitiveness in maintaining a favorable trade-off between noise suppression and detail retention.

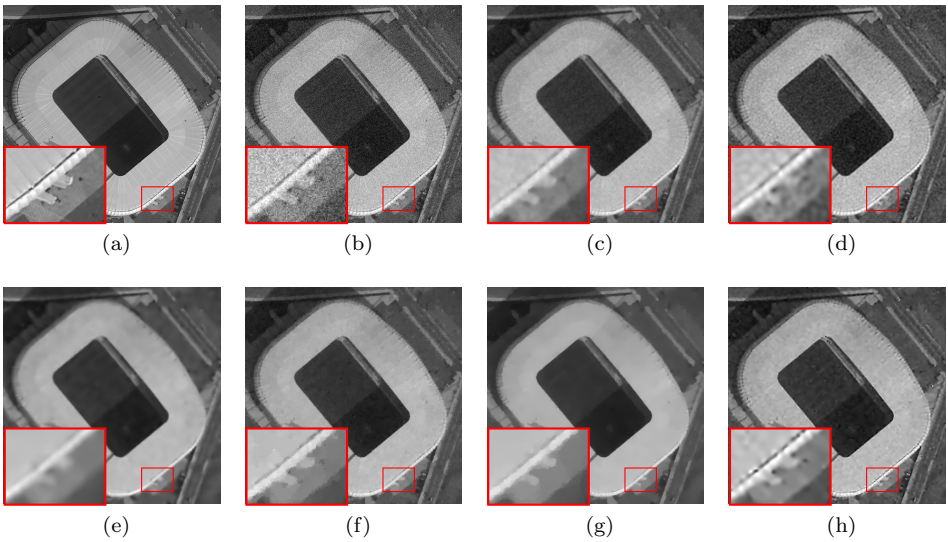


Fig. 8: Restored Stadium. (a)Original, (b)Degraded, (c)ROF model, (d)LLT model, (e)TGV model, (f)DBC-TV model, (g)Nesterov's method, and (h)Proposed method.

Finally, examination of the more complex stadium image in Figure 8 reveals that all methods deliver suboptimal denoising performance, resulting in image blurring and loss of details. Nonetheless, our proposed method demonstrates superior capability in restoring image details, preserving object contours, and notably enhancing the visibility of features such as the drain pipe and the chair.

Table 1: The restored results (PSNRs,SSIMs and FOMs) for 3×3 Gaussian blur kernel at noise levels $\sigma=10.$

	Image	ROF	LLT	TGV	DBC-TV	Nesterov	Proposed
	Cameraman	29.506/0.861/0.548	31.322/0.891/0.673	28.721/0.845/0.463	27.871/0.820/0.433	30.627/0.883/0.668	34.161/0.926/0.778
	Einstein	28.679/0.715/0.558	29.527/0.759/0.635	28.449/0.701/0.444	27.459/0.670/0.426	29.679/0.747/0.631	31.069/0.805/0.757
	Woman	33.450/0.893/ 0.618	34.731/0.917/0.592	34.160/0.896/0.432	32.150/0.882/0.524	34.375/0.900/0.590	35.589/0.919/0.557
	Peppers	27.795/0.851/0.762	28.592/0.877/0.806	26.909/0.827/0.668	26.607/0.818/0.700	30.234/0.782/0.694	31.363/0.913/0.877
	Butterfly	23.586/0.769/0.751	24.364/0.815/0.804	22.804/0.742/0.672	22.835/0.703/0.665	25.751/0.848/0.829	27.033/0.881/0.931
$\sigma = 10$	Starfish	24.757/0.745/0.725	25.959/0.796/0.754	24.238/0.709/0.622	23.337/0.671/0.637	25.644/0.779/0.772	28.491/0.870/0.912
0 = 10	Boat	26.510/0.696/0.573	27.389/0.734/0.645	25.838/0.664/0.472	25.313/0.644/0.455	27.261/0.728/0.643	29.359/0.799/0.822
	House	32.602/0.901/0.404	35.268/0.941/ 0.646	33.394/0.897/0.332	31.357/0.878/0.327	34.083/0.912/0.421	35.817 / 0.943 /0.523
	Text	18.560/0.728/0.744	18.977/0.711/0.756	18.286/0.771/0.746	18.846/0.826/0.754	19.609/0.872/0.777	22.681/0.873/0.828
	Logan	23.644/0.818/0.734	23.533/0.785/0.451	23.197/0.879/0.937	24.021/0.903/ 0.978	24.241/0.905/0.964	25.670 / 0.917 /0.762
	Stadium	27.900/0.756/0.557	27.890/0.747/ 0.636	27.137/0.709/0.338	27.616/0.729/0.444	28.743/0.768/0.504	$\mathbf{29.354/0.780}/0.548$
	Brain	28.435/0.726/0.549	28.350/0.698/ 0.625	27.470/0.745/0.314	28.425/0.764/0.366	29.281/0.800/0.470	30.642 / 0.802 /0.500

The foregoing analysis demonstrates the effectiveness and convergence of our proposed method. We further validate it through objective quantitative evaluations. These observations are supported by the results summarized in Tables 1-3. In these tables, the best values in each row are highlighted in boldface. Our method consistently achieves superior PSNR and competitive SSIM and FOM values across various noise

levels ($\sigma = 10, 20, 30$). For instance, at $\sigma = 10$, our method demonstrates superior performance over all competing methods, resulting in an average PSNR improvement of approximately 1.8 dB and an SSIM increase of 0.04. However, it exhibits slightly lower FOM values on images with fewer structural details and edge information, such as House, Logan, Stadium, and Brain, likely due to over-smoothing of subtle features. This leads to a minor reduction in FOM values.

Table 2: The denoising results(PSNRs,SSIMs and FOMs) for 3×3 Gaussian blur kernel at noise levels $\sigma = 20$.

	Image	ROF	LLT	TGV	DBC-TV	Nesterov's method	Proposed
	Cameraman	28.983/0.848/0.669	30.403/0.857/0.701	28.348/0.835/0.480	27.855/0.820/0.453	28.679/0.844/0.533	31.413/0.881/0.760
	Einstein	28.276/0.699/0.651	28.966/0.747/0.677	28.322/0.701/0.460	27.471/0.667/0.438	28.384/0.694/0.514	29.421/0.749/0.695
	Woman	32.041/0.850/0.676	33.032/0.882/0.664	33.808/0.896/0.466	31.947/0.874/0.556	32.514/0.877/ 0.577	33.946/0.897/0.493
	Peppers	27.019/0.811/0.801	28.002/0.851/0.811	26.678/0.822/0.668	26.518/0.810/0.709	28.741/0.751/0.662	29.221/0.869/0.873
	Butterfly	23.281/0.734/0.784	24.111/0.794/0.802	22.727/0.732/0.647	22.845/0.700/0.671	24.275/0.794/0.785	25.211/0.806/0.892
$\sigma = 20$	Starfish	24.446/0.720/0.738	25.600/0.783/0.801	24.046/0.700/0.648	23.342/0.669/0.623	24.124/0.708/0.699	26.346/0.799/0.873
v = 20	Boat	26.196/0.681/0.638	26.994/0.719/0.689	25.715/0.657/0.461	25.346/0.643/0.484	25.970/0.671/0.565	27.717/0.741/0.772
	House	31.508/0.882/0.511	32.713/0.894/ 0.586	32.032/0.883/0.308	31.201/0.875/0.314	32.172/0.885/0.355	33.567 / 0.912 /0.476
	Text	18.433/0.561/0.747	18.886/0.537/0.757	18.308/0.783/0.744	18.770/ 0.808 /0.771	18.925/0.796/0.763	21.969 /0.638/ 0.828
	Logan	23.358/0.695/0.518	23.308/0.652/0.320	23.140/0.849/ 0.950	23.852/0.870/0.933	23.734/ 0.874 /0.949	25.092 /0.764/0.452
	Stadium	27.487/0.717/0.674	27.297/0.697/0.672	27.296/0.718/0.372	27.589/0.719/0.367	27.566/0.729/0.435	28.607/0.760/0.694
	Brain	27.833/0.613/0.481	27.696/0.566/ 0.614	27.540/0.713/0.356	28.188/0.727/0.399	28.149/ 0.743 /0.381	29.653 /0.682/0.504

At higher noise levels ($\sigma=20$ and $\sigma=30$), although the PSNR advantage of our method persists, the margins narrow and the SSIM and FOM metrics reveal mixed performance compared to other approaches such as LLT, TGV, and DBC-TV. This trend suggests that while our method effectively balances noise reduction and edge preservation in moderately noisy conditions, its relative advantage diminishes under severe noise contamination, possibly reflecting the intrinsic limitations of the hybrid modeling approach.

Table 3: The denoising results(PSNRs,SSIMs and FOMs) for 3×3 Gaussian blur kernel at noise levels $\sigma = 30$.

	Image	ROF	LLT	TGV	DBC-TV	Nesterov's method	Proposed
$\sigma = 30$	Cameraman	27.721/0.813/0.617	28.628/0.758/0.603	27.282/0.810/0.405	27.826/0.820/0.437	27.536/0.820/0.479	29.892/0.842/0.713
	Einstein	27.268/0.659/0.609	27.729/0.687/ 0.706	28.061/0.699/0.527	27.494/0.664/0.488	27.666/0.671/0.520	28.278 / 0.711 /0.637
	Woman	30.661/0.817/ 0.634	30.275/0.780/0.492	32.133/0.883/0.503	31.672/0.864/0.590	31.750/0.867/0.558	32.367 / 0.886 /0.559
	Peppers	25.677/0.762/0.792	26.778/0.783/0.828	25.795/0.790/0.653	26.391/0.802/0.718	27.014/0.737/0.665	27.504/0.828/0.841
	Butterfly	22.343/0.676/0.743	23.566/0.746/0.829	22.698/0.727/0.715	22.853/0.697/0.679	23.246/0.760/0.774	23.914/0.766/0.835
	Starfish	23.428/0.666/0.753	24.858/0.741/0.806	23.051/0.651/0.574	23.359/0.667/0.651	23.180/0.657/0.665	24.911/0.746/0.866
	Boat	25.316/0.640/0.631	26.144/0.670/ 0.762	25.082/0.635/0.443	25.389/0.643/0.484	25.091/0.634/0.502	26.475 / 0.693 /0.700
	House	30.134/0.852/0.477	30.940/0.865/ 0.512	31.595/0.871/0.473	30.994/0.871/0.325	31.101/0.874/0.350	$\mathbf{31.884/0.889}/0.375$
	Text	18.296/0.445/0.751	18.718/0.422/0.765	18.162/0.598/0.749	18.600/ 0.997 /0.756	18.291/0.723/0.743	21.033 /0.484/ 0.824
	Logan	23.143/0.612/0.450	22.986/0.543/0.276	22.891/0.692/0.591	23.504/ 0.861 /0.930	23.226/0.843/ 0.939	24.414 /0.679/0.455
	Stadium	26.892/0.666/0.640	$26.892/0.666/\boldsymbol{0.640}$	27.089/0.697/0.564	27.126/0.717/0.386	26.889/0.709/0.398	27.518 / 0.722 /0.529
	Brain	27.112/0.519/0.597	26.821/0.474/ 0.567	27.274/0.599/0.521	27.562/ 0.725 /0.388	27.190/0.696/0.351	28.475 /0.597/0.482

Overall, across all three noise levels, our proposed method consistently achieves the highest PSNR values, with average gains of approximately 1.8 dB, 1.26 dB, and 1.03 dB over competing TV-based approaches for all tested images. It also attains superior SSIM performance in most cases, particularly for images characterized by sharp edges and rich textures, such as Peppers, Butterfly, and Starfish. Conversely, it exhibits marginally lower FOM values on smoother images (e.g., House, Logan, Stadium, Brain), especially at elevated noise levels. Under the most severe noise condition ($\sigma = 30$), both SSIM and FOM metrics indicate inferior performance relative

to LLT, TGV, and DBC-TV models, suggesting that the method's effectiveness in preserving precise edge structures diminishes as noise level increases.

These findings collectively validate the effectiveness and denoising capability of our approach across a diverse range of image types, demonstrating a consistent ability to suppress noise while preserving crucial edge and texture details. At the same time, the results delineate the constraints of the proposed method in maintaining fine edge preservation when confronted with extreme noise degradation, highlighting areas for potential future improvement.

Table 4: The denoising results (PSNRs, SSIMs and FOMs) for 3×3 Gaussian blur kernel at noise levels $\sigma = 20$.

	Image	DRUNet	FFDNet	DnCNN	DPIR	Proposed
	Cameraman	28.922 / 0.862 / 0.842	28.753 / 0.857 / 0.832	27.904 / 0.821 / 0.793	31.356 / 0.884 / 0.684	31.413 / 0.881 / 0.760
	Einstein	29.115 / 0.737 / 0.708	$28.956 \; / \; 0.731 \; / \; 0.674$	$28.001\ /\ 0.675\ /\ 0.584$	$30.049 \ / \ 0.756 \ / \ 0.649$	$29.421 \ / \ 0.749 \ / \ 0.695$
	Woman	$34.574 \ / \ 0.903 \ / \ 0.752$	$34.304 \; / \; 0.899 \; / \; 0.711$	$33.366\ /\ 0.884\ /\ 0.681$	$34.987 \; / \; 0.905 \; / \; 0.533$	$33.946 \ / \ 0.897 \ / \ 0.493$
	Peppers	$29.592\ /\ 0.775\ /\ 0.841$	$29.485\ /\ 0.772\ /\ 0.824$	$28.897\ /\ 0.754\ /\ 0.787$	30.817 / 0.790 / 0.801	$29.221 \; / \; 0.869 \; / \; 0.873$
	Butterfly	$24.016\ /\ 0.803\ /\ 0.876$	$23.894 \; / \; 0.798 \; / \; 0.872$	$23.477\ /\ 0.771\ /\ 0.801$	$27.026 \; / \; 0.871 \; / \; 0.866$	$25.211\ /\ 0.806\ /\ \textbf{0.892}$
$\sigma = 20$	Starfish	$24.667\ /\ 0.735\ /\ 0.766$	$24.415\ /\ 0.724\ /\ 0.747$	$23.738\ /\ 0.676\ /\ 0.646$	$26.017 \; / \; 0.785 \; / \; 0.789$	$26.346 \; / \; 0.799 \; / \; 0.873$
0 = 20	Boat	$26.224 \; / \; 0.695 \; / \; 0.710$	26.094 / 0.688 / 0.700	$25.349 \; / \; 0.637 \; / \; 0.624$	27.407 / 0.730 / 0.669	$27.717 \; / \; 0.741 \; / \; 0.772$
	House	$34.561 \ / \ 0.911 \ / \ 0.873$	34.203 / 0.905 / 0.889	$33.056 \; / \; 0.882 \; / \; 0.818$	35.651 / 0.913 / 0.402	$33.567 \; / \; 0.912 \; / \; 0.476$
	Text	17.271 / 0.846 / 0.746	$16.972 \; / \; 0.822 \; / \; 0.742$	$16.715\ /\ 0.357\ /\ 0.734$	22.976 / 0.968 / 0.864	$21.969 \; / \; 0.638 \; / \; 0.828$
	Logan	$22.516\ /\ 0.915\ /\ 0.824$	$22.536 \; / \; 0.906 \; / \; \textbf{0.974}$	$22.358 \; / \; 0.589 \; / \; 0.973$	$27.158 \; / \; 0.970 \; / \; 0.966$	$25.092\ /\ 0.764\ /\ 0.452$
	Stadium	$27.711 \; / \; 0.740 \; / \; \textbf{0.713}$	$27.577 \; / \; 0.730 \; / \; 0.669$	$26.868\ /\ 0.697\ /\ 0.518$	$28.601 \; / \; 0.758 \; / \; 0.533$	$28.607 \; / \; 0.760 \; / \; 0.694$
	Brain	27.769 / 0.796 / 0.843	$27.693\ /\ 0.788\ /\ 0.826$	$26.996\ /\ 0.439\ /\ 0.821$	$30.232 \ / \ 0.822 \ / \ 0.423$	$29.653\ /\ 0.682\ /\ 0.504$
	Average	27.245 / 0.810 / 0.791	27.074 / 0.802 / 0.788	26.567 / 0.706 / 0.731	28.693 / 0.845 / 0.681	28.935 / 0.791 / 0.682

Furthermore, we compare our method with several representative learning-based models, including DRUNet [39], FFDNet [40], DnCNN [38], and the Plug-and-Play method DPIR [37].

As shown in Table 4, the proposed method achieves the highest average PSNR value. Compared with learning-based models, our approach improves the average PSNR by approximately 1.86 dB, 1.69 dB, and 2.23 dB, respectively, while also achieving a 0.24 dB improvement over the DPIR method. The corresponding visual comparisons are presented in Figure 9.

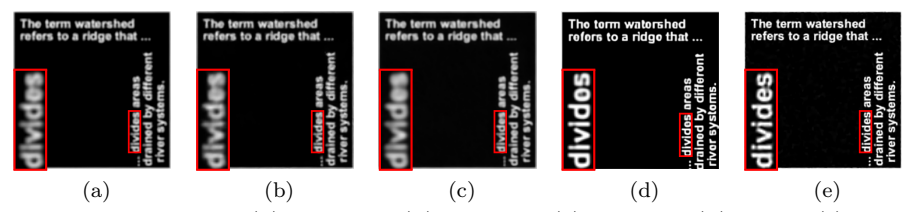


Fig. 9: Restored Text. (a)DRUNet, (b)FFDNet, (c)DnCNN, (d)DPIR, (f)Proposed method.

For the Text image, our proposed method obtains relatively higher PSNR and FOM values. Although the metrics are slightly lower than those of the DPIR method, the visual comparison indicates that DPIR introduces noticeable distortions. For instance, the word "divides" is incorrectly restored as "dlvldos". In contrast, our method successfully preserves the structural properties of the word "divides", demonstrating its superior accuracy.

In summary, the qualitative and quantitative analyses substantiate the effectiveness of our proposed method in image restoration tasks. Compared with classical TV-

based methods as well as representative learning-based models, our method achieves superior performance in both visual quality and quantitative metrics, thereby affirming its practical utility and competitiveness among current state-of-the-art techniques.

5. Conclusion. In this paper, we proposed a novel semi-convergent stage-wise framework for adaptive total variation regularization, which effectively leverages the complementary strengths of both first- and higher-order TV regularizers. The convergence of the stage-wise alternating method was established both theoretically and numerically. Extensive experiments demonstrate that the proposed method outperforms classical TV-based approaches and several learning-based methods in terms of PSNR, SSIM, and FOM metrics. Both visual and quantitative results confirm the superiority of the proposed method in preserving fine details, yielding restored images that are visually pleasing and quantitatively robust. Nevertheless, some limitations remain, particularly under severe noise conditions, where the effectiveness of the proposed method is somewhat diminished. This suggests potential room for improvement in the design and integration of TV-based models. Future work will explore the extension of the hybrid alternating optimization framework to other advanced regularization models, aiming to further enhance restoration quality and computational efficiency. The promising results obtained in this study lay a solid foundation for such developments.

REFERENCES

- T. Adam, M. F. Hassan, and R. Paramesran, A study on staircase artifacts in total variation image restoration, in 2021 IEEE International Conference on Signal and Image Processing Applications (ICSIPA), IEEE, 2021, pp. 83–88.
- T. Adam and R. Paramesran, Image denoising using combined higher order non-convex total variation with overlapping group sparsity, Multidimensional Systems and Signal Processing, 30 (2019), pp. 503–527.
- [3] T. ADAM, R. PARAMESRAN, Y. MINGMING, AND K. RATNAVELU, Combined higher order nonconvex total variation with overlapping group sparsity for impulse noise removal, Multimedia Tools and Applications, 80 (2021), pp. 18503–18530.
- [4] L. Afraites, A. Hadri, A. Laghrib, and M. Nachaoui, A weighted parameter identification pde-constrained optimization for inverse image denoising problem, The Visual Computer, 38 (2022), pp. 2883–2898.
- [5] I. BAKUROV, M. BUZZELLI, R. SCHETTINI, M. CASTELLI, AND L. VANNESCHI, Structural similarity index (ssim) revisited: A data-driven approach, Expert Systems with Applications, 189 (2022), p. 116087.
- [6] A. Beck, L. Tetruashvili, Y. Vaisbourd, and A. Shemtov, Rate of convergence analysis of dual-based variables decomposition methods for strongly convex problems, Operations Research Letters, 44 (2016), pp. 61–66.
- [7] D. BÉRÉZIAT AND I. HERLIN, Solving ill-posed image processing problems using data assimilation, Numerical Algorithms, 56 (2011), pp. 219–252.
- [8] J. A. BHUTTO, A. KHAN, AND Z. RAHMAN, Image restoration with fractional-order total variation regularization and group sparsity, Mathematics, 11 (2023), p. 3302.
- [9] K. Bredies, K. Kunisch, and T. Pock, Total generalized variation, SIAM Journal on Imaging Sciences, 3 (2010), pp. 492–526.
- [10] K. Bredies and D. A. Lorenz, Linear convergence of iterative soft-thresholding, Journal of Fourier Analysis and Applications, 14 (2008), pp. 813–837.
- [11] H. CHEN, C. QU, Y. ZHANG, C. CHEN, AND J. JIAO, Multi-view self-supervised disentanglement for general image denoising, in Proceedings of the IEEE/CVF International Conference on Computer Vision, 2023, pp. 12281–12291.
- [12] A. DE MARCHI, X. JIA, C. KANZOW, AND P. MEHLITZ, Constrained composite optimization and augmented lagrangian methods, Mathematical Programming, 201 (2023), pp. 863–896.
- [13] J. Guo and Q. Chen, Image denoising based on nonconvex anisotropic total-variation regularization, Signal Processing, 186 (2021), p. 108124.
- [14] D. HAN AND X. YUAN, A note on the alternating direction method of multipliers, Journal of

- Optimization Theory and Applications, 155 (2012), pp. 227-238.
- [15] M. HINTERMÜLLER AND C. N. RAUTENBERG, Optimal selection of the regularization function in a weighted total variation model. part i: Modelling and theory, Journal of Mathematical Imaging and Vision, 59 (2017), pp. 498–514.
- [16] M. HONG AND Z.-Q. Luo, On the linear convergence of the alternating direction method of multipliers, Mathematical Programming, 162 (2017), pp. 165–199.
- [17] K. Jon, Y. Sun, Q. Li, J. Liu, X. Wang, and W. Zhu, Image restoration using overlapping group sparsity on hyper-laplacian prior of image gradient, Neurocomputing, 420 (2021), pp. 57-69.
- [18] M. A. KHAN, W. CHEN, A. ULLAH, AND Z. Fu, A mesh-free algorithm for rof model, EURASIP Journal on Advances in Signal Processing, 2017 (2017), pp. 1–16.
- [19] F. LI, C. SHEN, J. FAN, AND C. SHEN, Image restoration combining a total variational filter and a fourth-order filter, Journal of Visual Communication and Image Representation, 18 (2007), pp. 322–330.
- [20] J. LIU, T.-Z. HUANG, I. W. SELESNICK, X.-G. LV, AND P.-Y. CHEN, Image restoration using total variation with overlapping group sparsity, Information Sciences, 295 (2015), pp. 232– 246
- [21] M. LYSAKER, A. LUNDERVOLD, AND X.-C. TAI, Noise removal using fourth-order partial differential equation with applications to medical magnetic resonance images in space and time, IEEE Transactions on image processing, 12 (2003), pp. 1579–1590.
- [22] M. LYSAKER AND X.-C. TAI, Iterative image restoration combining total variation minimization and a second-order functional, International journal of computer vision, 66 (2006), pp. 5– 18.
- [23] A. MOZHAEVA, L. STREETER, I. VLASUYK, AND A. POTASHNIKOV, Full reference video quality assessment metric on base human visual system consistent with psnr, in 2021 28th Conference of Open Innovations Association (FRUCT), IEEE, 2021, pp. 309–315.
- [24] S. Mukherjee, J. Farrand, and W. Yao, A study of total-variation based noise reduction algorithms for low-dose cone-beam computed tomography, Int. J. Image Process, 10 (2016), pp. 188–204.
- [25] A. NASONOV AND A. KRYLOV, An improvement of bm3d image denoising and deblurring algorithm by generalized total variation, in 2018 7th European workshop on visual information processing (EUVIP), IEEE, 2018, pp. 1–4.
- [26] S. OH, H. WOO, S. YUN, AND M. KANG, Non-convex hybrid total variation for image denoising, Journal of Visual Communication and Image Representation, 24 (2013), pp. 332–344.
- [27] Z.-F. Pang, L.-L. Wang, and Y.-F. Yang, The proximal point method for a hybrid model in image restoration, arXiv preprint arXiv:1110.1804, (2011).
- [28] K. Papafitsoros, Novel higher order regularisation methods for image reconstruction, PhD thesis, 2015.
- [29] K. Papafitsoros and C.-B. Schönlieb, A combined first and second order variational approach for image reconstruction, Journal of mathematical imaging and vision, 48 (2014), pp. 308–338.
- [30] L. I. RUDIN, S. OSHER, AND E. FATEMI, Nonlinear total variation based noise removal algorithms, Physica D: nonlinear phenomena, 60 (1992), pp. 259–268.
- [31] Y. WANG, J. YANG, W. YIN, AND Y. ZHANG, A new alternating minimization algorithm for total variation image reconstruction, SIAM Journal on Imaging Sciences, 1 (2008), pp. 248– 272.
- [32] C. Wu and X.-C. Tai, Augmented lagrangian method, dual methods, and split bregman iteration for rof, vectorial tv, and high order models, SIAM Journal on Imaging Sciences, 3 (2010), pp. 300–339.
- [33] J. XIANG, H. XIANG, AND L. WANG, Poisson noise image restoration method based on variational regularization, Signal, Image and Video Processing, 17 (2023), pp. 1555–1562.
- [34] W.-S. XIE, Y.-F. YANG, AND B. ZHOU, An admm algorithm for second-order tv-based mr image reconstruction, Numerical Algorithms, 67 (2014), pp. 827–843.
- [35] J. Xu, X. Feng, and Y. Hao, A coupled variational model for image denoising using a duality strategy and split bregman, Multidimensional systems and signal processing, 25 (2014), pp. 83–94.
- [36] M. Yin, T. Adam, R. Paramesran, and M. F. Hassan, An l0-overlapping group sparse total variation for impulse noise image restoration, Signal Processing: Image Communication, 102 (2022), p. 116620.
- [37] K. ZHANG, Y. LI, W. ZUO, L. ZHANG, L. VAN GOOL, AND R. TIMOFTE, Plug-and-play image restoration with deep denoiser prior, IEEE Transactions on Pattern Analysis and Machine Intelligence, 44 (2021), pp. 6360–6376.

- [38] K. Zhang, W. Zuo, Y. Chen, D. Meng, and L. Zhang, Beyond a gaussian denoiser: Residual learning of deep cnn for image denoising, IEEE transactions on image processing, 26 (2017), pp. 3142–3155.
- [39] K. ZHANG, W. ZUO, S. GU, AND L. ZHANG, Learning deep cnn denoiser prior for image restoration, in Proceedings of the IEEE conference on computer vision and pattern recognition, 2017, pp. 3929–3938.
- [40] K. ZHANG, W. ZUO, AND L. ZHANG, Ffdnet: Toward a fast and flexible solution for cnn-based image denoising, IEEE Transactions on Image Processing, 27 (2018), pp. 4608–4622.
- [41] W. Zhang, Y. Zhao, T. P. Breckon, and L. Chen, Noise robust image edge detection based upon the automatic anisotropic gaussian kernels, Pattern Recognition, 63 (2017), pp. 193– 205